Technologies **2015**, *3*, 219-237; doi:10.3390/technologies3040219

OPEN ACCESS

technologies

ISSN 2227-7080

www.mdpi.com/journal/technologies

Article

A New Compton Camera Imaging Model to Mitigate the Finite Spatial Resolution of Detectors and New Camera Designs for Implementation

Bruce Smith

Department of Electrical and Computer Engineering, University of Texas at San Antonio, One UTSA Circle, San Antonio, TX 78249, USA; E-Mail: Bruce.Smith@utsa.edu or Bruce.Smith@IEEE.org; Tel.: +1-210-458-5512; Fax: +1-210-458-5947

Academic Editors: Yudong Zhang and Zhengchao Dong

Received: 26 June 2015 / Accepted: 21 October 2015 / Published: 27 October 2015

Abstract: An intrinsic limitation of the accuracy that can be achieved with Compton cameras results from the inevitable fact that the detectors, which comprise the camera, cannot have infinitely-accurate spatial resolution. To mitigate this loss of accuracy, a new imaging model is proposed. The implementation of the new imaging model, however, requires new camera designs. The results of a computer simulation indicate that the new imaging model can produce reasonable images, at least when noiseless simulated data are used. In the future, more work is needed to determine if the use of the new imaging model will improve the imaging capabilities of Compton cameras despite the loss of sensitivity caused by the use of the new camera designs. Regardless of the outcome of this work, the results presented here illustrate that new models for imaging from Compton scatters are possible and motivate the development of further models that could be more advantageous than the ones already developed.

Keywords: medical imaging; emission tomography; nuclear medicine; single-photon emission computed tomography

1. Introduction

Compton cameras have the potential to significantly improve diagnostic and therapeutic medicine. For instance, bismuth-213 radioimmunotherapy is actively being pursued at the present time for treating various forms of cancer [1–30], as well as HIV [31,32]. Maximizing the efficacy of this treatment

requires maximizing the amount of dose administered to the patient. However, the potential hazard to bone marrow, kidney, lungs and other secondary organs limits the dose that can be administered. The amount of radioactivity that can be tolerated by these secondary organs varies from patient to patient. Hence, accurately calculating the absorbed dose within these organs is essential. Producing the most accurate images possible of the bismuth in the patient will result in the most accurate calculations of absorbed dose. Of all the medical imaging techniques presently available, single-photon emission computed tomography (SPECT) will produce the best possible images of bismuth-213. However, the collimator that is used in a SPECT camera limits the energy of the photons that can be imaged. As a consequence, in comparison to images of technetium-99m (140 keV), a SPECT camera will produce relatively poor quality images of bismuth-213 because of the high energy of the photons (440 keV) that it emits. Fortunately, since collimators are not used, Compton cameras have the potential of out-performing a SPECT camera when bismuth-213 is imaged.

An intrinsic limitation of the accuracy that can be achieved with Compton cameras results from the inevitable fact that the detectors, which comprise the camera, cannot have infinitely-accurate spatial resolution. The effects of the finite spatial resolution of detectors, the finite energy resolution of detectors and a phenomenon known as Doppler broadening on the image accuracy of Compton cameras have been studied [33]. It was found that of these three factors, finite spatial resolution is the dominant degrading factor at a higher medical diagnostic energy level (511 keV). The new theory presented in this paper may mitigate the loss of accuracy due to the finite spatial resolution of the detectors. In addition, this theory, if fully developed (generalized), has the potential to decrease the amount of data that need to be processed and provides more flexibility in designing the detectors that comprise the camera. The new theory is based on a new imaging model. In Section 3 of this paper, this new imaging model is developed along with a method for reconstructing an integral of a distribution of radioactivity along a line using the new imaging model. New camera designs that can be used to exploit the new imaging model are presented in Section 4 of this paper. First, a camera design that can be used to produce a parallel projection of the distribution is presented. Since this parallel projection is similar to the data obtained by a conventional SPECT camera equipped with a parallel hole collimator at one positioning of the camera, three-dimensional reconstructions could be obtained by producing such projections as the Compton camera is rotated about the patient. A second design is presented that allows fan-beam projections of the distribution to be reconstructed. Producing fan-beam projections as the camera is rotated about the distribution would, of course, allow two-dimensional reconstructions to be made. The results of computer simulations to demonstrate the imaging model and inversion method developed in Section 3 are presented in Section 6. Finally, in Section 7, the advantages and disadvantages of new the imaging model and the new camera designs are discussed.

2. Existing Compton Camera Imaging Models

As originally proposed, a Compton camera consists of two parallel planar detectors [34]. Ideally, the physics within the camera is as follows. As illustrated in Figure 1, a photon, which originated within the distribution, interacts, via a Compton scatter, with the nearest of the two detectors. As a result of the

scatter, the photon loses some of its energy, and the direction of its trajectory changes. Then, the photon continues on in the new direction and interacts with the second detector.

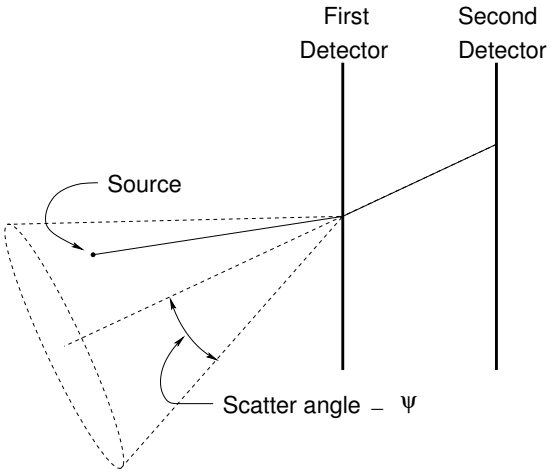

Figure 1. Illustration of the ideal physics of Compton cameras.

Assuming this camera physics, the following is done to construct data so that the distribution of radioactivity can be estimated. The location of the two points of interaction of the photon and the amount of energy lost during the scatter are measured. The photons that interact at a given location on the first detector and a given location on the second detector and that have lost a given amount of energy are tallied. This provides the number of counts in a "measurement bin".

Two imaging models for Compton camera data have been proposed by other researchers. Both models assume that the number of counts in a measurement bin is proportional to an integral of the distribution over a cone. The apex of the cone is at the first point of interaction; the axis of symmetry of the cone is the line that connects the two points of interaction; and the half angle of the cone is the scatter angle calculated from the energy measurement using Compton's law [35]. These imaging models were proposed in an effort to develop reconstruction methods that would produce a three-dimensional estimate of the distribution of radioactivity from a set of such integrals.

The two models use different mathematical equations to express the integral over the cone. One model considered the data to be a surface integral of the distribution over a cone [36]. The reader is reminded that not all integrals over a surface are surface integrals. For $\mathbf{\Phi} \in \mathbb{R}^3$, $\boldsymbol{\beta} \in S^2$ and $0 < \psi < \pi$, let the symbol $\mathrm{S}_{\mathrm{SI}}(\mathbf{\Phi}, \boldsymbol{\beta}, \psi)$ denote the surface integral (SI) model of the distribution of radioactivity on the one sheet cone whose apex is the point: $\mathbf{\Phi}$, the axis of symmetry is the unit vector: $\boldsymbol{\beta}$, and the half angle is: ψ. Furthermore, let $f(\mathbf{x})$ denote the distribution of radioactivity at the point $\mathbf{x}$ for: $\mathbf{x} \in \mathbb{R}^3$. Let the vectors: $\mathbf{\Phi}$, $\boldsymbol{\beta}$, and: $\mathbf{x}$ be described in terms of a global coordinate system. A local coordinate system in which the "z" axis points in the direction of the vector $\boldsymbol{\beta}$ is used in expressing the surface integral. Using this coordinate system, the unit vector $\boldsymbol{\alpha} = \boldsymbol{\alpha}(\phi, \psi)$ is expressed in a spherical coordinate system by letting:

$$\boldsymbol{\alpha} \triangleq (\cos\phi \sin\psi, \sin\phi \sin\psi, \cos\psi)^{\top} \tag{1}$$

where ψ is the angle measured from the "z" axis. A standard calculus equation for the surface integral of a cone yields:

$$\mathrm{S_{SI}}(\boldsymbol{\Phi}, \boldsymbol{\beta}, \psi) = \sin\psi \int_{\phi=0}^{2\pi} \int_{r=0}^{\infty} f\Big(\boldsymbol{\Phi} + r M^{\top} \boldsymbol{\alpha}(\phi, \psi)\Big) r \, dr \, d\phi \tag{2}$$

where the rotation matrix $M^{\top}$ is defined as:

$$M^{\top} = \Big[\boldsymbol{\beta_{\perp 1}} \Big| \boldsymbol{\beta_{\perp 2}} \Big| \boldsymbol{\beta}\Big] \tag{3}$$

where $\boldsymbol{\beta}$, $\boldsymbol{\beta_{\perp 1}}$ and $\boldsymbol{\beta_{\perp 2}}$ are three orthonormal column vectors in $\mathbb{R}^3$.

A second model of the data has been considered [37]. This model is called the integral of cone-beam line-integrals (ILI) model here. Let $\mathrm{S_{ILI}}(\boldsymbol{\Phi}, \boldsymbol{\beta}, \psi)$ denote the integral of cone-beam line-integrals of the distribution of radioactivity. The cone-beam line-integrals of the distribution at: $\boldsymbol{\Phi}$ is defined as:

$$g(\boldsymbol{\Phi}, \boldsymbol{\nu}) = \int_{0}^{\infty} f\Big(\boldsymbol{\Phi} + t \, \boldsymbol{\nu}\Big) \, dt \tag{4}$$

where: $|\boldsymbol{\nu}| = 1$. Using: $M^{\top}$ and: $\boldsymbol{\alpha}(\phi, \psi)$ as previously defined, the integral of cone-beam line-integrals of the distribution is defined as:

$$\mathrm{S_{ILI}}(\boldsymbol{\Phi}, \boldsymbol{\beta}, \psi) = \int_{0}^{2\pi} g\Big(\boldsymbol{\Phi}, M^{\top} \boldsymbol{\alpha}(\phi, \psi)\Big) \, d\phi \tag{5}$$

In a previous publication, conditions that describe the data needed to reconstruct a single line-integral from Compton camera data were developed [38]. It was found there that these "completeness conditions" depended on which of the two models was assumed for the data. In particular, it was found that the completeness condition for the SI model is more demanding than the ILI condition, because the SI condition needed data from more than one apex, whereas the ILI condition needed data from just one apex. Like the ILI model, the new imaging model that will be proposed in the next section will have the same desirable property.

3. The Development of A New Imaging Model and Its Inversion

To develop the new imaging model, a new function is defined. For $\boldsymbol{\beta} \in S^2$ and $\ell \in \mathbb{R}^1$, the function $F(\boldsymbol{\beta}, \ell)$ is defined as: [39]:

$$F(\boldsymbol{\beta}, \ell) = \frac{1}{\pi} \lim_{\epsilon \to 0} \int_{-\infty}^{+\infty} H_{\epsilon}(\ell - t) \check{f}(\boldsymbol{\beta}, t) \, dt \tag{6}$$

where:

$$H_{\epsilon}(t) = \begin{cases} \dfrac{1}{\epsilon^2}, & \text{for } |t| < \epsilon; \\ \dfrac{-1}{t^2}, & \text{for } |t| \geq \epsilon \end{cases} \tag{7}$$

and $\check{f}(\boldsymbol{\beta}, \ell)$ is the three-dimensional Radon transform; namely,

$$\check{f}(\boldsymbol{\beta}, \ell) \triangleq \int_{-\infty}^{\infty} \int_{-\infty}^{\infty} f(\ell\,\boldsymbol{\beta} + s\boldsymbol{\beta}_{\perp \mathbf{1}} + t\boldsymbol{\beta}_{\perp \mathbf{2}})\, ds\, dt \tag{8}$$

In words, $F(\boldsymbol{\beta}, \ell)$ is the Hilbert transform of the partial derivative of the three-dimensional Radon transform.

To define a line-integral of the distribution, the following two unit vectors are defined in the global coordinate system:

$$\boldsymbol{\varphi} = (\cos\varphi, \sin\varphi, 0)^{\top} \quad \text{and} \quad \boldsymbol{\varphi}_{\perp} = (-\sin\varphi, \cos\varphi, 0)^{\top} \tag{9}$$

Let: $P(\boldsymbol{\Phi}, \boldsymbol{\varphi})$ be the integral of the distribution along the line parallel to the vector: $\boldsymbol{\varphi}_{\perp}$ that intersects $\boldsymbol{\Phi}$; that is,

$$P(\boldsymbol{\Phi}, \boldsymbol{\varphi}) \triangleq \int_{-\infty}^{\infty} f(\boldsymbol{\Phi} + s\boldsymbol{\varphi}_{\perp})\, ds \tag{10}$$

The function $P(\boldsymbol{\Phi}, \boldsymbol{\varphi})$ can be obtained from $F(\boldsymbol{\beta}, \ell)$ via Equation (5.2) in [39]; namely,

$$P(\boldsymbol{\Phi}, \boldsymbol{\varphi}) = \frac{1}{2\pi} \int_{0}^{\pi} F(\boldsymbol{\beta}(\theta, \varphi), \boldsymbol{\Phi} \cdot \boldsymbol{\beta}(\theta, \varphi))\, d\theta \tag{11}$$

where:

$$\boldsymbol{\beta}(\theta, \varphi) = (\cos\varphi \sin\theta, \sin\varphi \sin\theta, \cos\theta)^{\top} \tag{12}$$

Lemma 1.

$$F(\boldsymbol{\beta}, \boldsymbol{\Phi} \cdot \boldsymbol{\beta}) = \frac{1}{\pi} \lim_{\epsilon \to 0} \int_{0}^{\pi} \mathrm{S}_{\mathrm{ILI}}(\boldsymbol{\Phi}, \boldsymbol{\beta}, \psi) H_{\epsilon}(\cos\psi) \sin\psi\, d\psi \tag{13}$$

The proof of Lemma 1 is given in [40].

Substituting Equation (13) into Equation (11) yields:

$$P(\boldsymbol{\Phi}, \boldsymbol{\varphi}) = \frac{1}{2\pi^2} \int_{0}^{\pi} \lim_{\epsilon \to 0} \int_{0}^{\pi} \mathrm{S}_{\mathrm{ILI}}(\boldsymbol{\Phi}, \boldsymbol{\beta}(\theta, \varphi), \psi) H_{\epsilon}(\cos\psi) \sin\psi\, d\psi\, d\theta \tag{14}$$

Exchanging integrals yields:

$$P(\mathbf{\Phi}, \boldsymbol{\varphi}) = \frac{1}{2\pi^2} \int_0^\pi \lim_{\epsilon \to 0} \int_0^\pi \mathrm{S}_{\mathrm{ILI}}(\mathbf{\Phi}, \boldsymbol{\beta}(\theta, \varphi), \psi)\, d\theta\, H_\epsilon(\cos\psi) \sin\psi\, d\psi \tag{15}$$

The new imaging model is defined as:

$$\mathrm{S}_{\mathrm{IILI}}(\mathbf{\Phi}, \boldsymbol{\varphi}, \psi) = \int_0^\pi \mathrm{S}_{\mathrm{ILI}}(\mathbf{\Phi}, \boldsymbol{\beta}(\theta, \varphi), \psi)\, d\theta \tag{16}$$

This model is referred to as the integral of the integral of cone-beam line-integrals (IILI) model. Substituting Equation (16) into Equation (15) yields:

$$P(\mathbf{\Phi}, \boldsymbol{\varphi}) = \frac{1}{2\pi^2} \lim_{\epsilon \to 0} \int_0^\pi \mathrm{S}_{\mathrm{IILI}}(\mathbf{\Phi}, \boldsymbol{\varphi}, \psi) H_\epsilon(\cos\psi) \sin\psi\, d\psi \tag{17}$$

The above equation makes it possible to invert the IILI model to obtain the integral of the distribution along the line parallel to the vector: $\boldsymbol{\varphi}_\perp$ that intersects $\mathbf{\Phi}$.

Developing a geometric interpretation of the last two equations is useful. The geometric interpretation of Equation (17) is relatively straightforward. The integral of the distribution along the line parallel to the vector: $\boldsymbol{\varphi}_\perp$ that intersects the apex $\mathbf{\Phi}$ can be calculated by integrating the appropriately-weighted IILI model over all possible half-angles. To interpret the new imaging model defined in Equation (16), it is helpful to determine the set of cones that are involved with the equation's integral. Equation (16) involves the integral of conical integrals where the ILI model is used for the conical integrals. Since $\mathbf{\Phi}$ and ψ are fixed in Equation (16), the cones that are being integrated over share a common apex and half-angle. Moreover, all of these cones have an axis of symmetry that is perpendicular to the vector: $\boldsymbol{\varphi}_\perp$. Since the integral in Equation (16) has a lower limit of zero and an upper limit of π, to implement this integral, the conical integrals for the previously-described set of cones for a collection of axes that span 180 degrees are needed. In other words then, Equation (16) involves integrating the conical integrals over the set of cones with a fixed half-angle that share a common apex $\mathbf{\Phi}$ and have axes perpendicular to the vector: $\boldsymbol{\varphi}_\perp$ and span 180 degrees around the vector. Camera designs that make it possible to obtain this integral of conical integrals are discussed in the next section.

4. Camera Designs to Exploit the New Imaging Model

4.1. Reconstruction Using the New Imaging Model

The new imaging model being proposed here can be implemented using the camera design illustrated in Figure 2. In this design, the first detector consists of a single detector element and is surrounded by a coplanar semicircle-shaped second detector. In what follows, this design will be called the single first semicircle second (SFSS) design. Recall from Section 3, to reconstruct the line through the distribution using the new imaging model, the conical integrals over a set of cones with a fixed half-angle that share

a common apex lying on the line and have axes perpendicular to the line and span 180 degrees around the line need to be integrated. This can be achieved with the SFSS design, because the first detector element can be "seen" from the second detector in a "semicircle of directions". Because the second detector consists of just one element, the physics within the camera would in effect implement the integral in Equation (16). In this case, a measurement bin is defined as the number of photons that interact with the single first detector element, loses a certain amount of energy and then interacts anywhere on the semicircle-shaped second detector. If these measurement bins are obtained for all possible energies, then the function $\mathrm{S}_{\mathrm{IILI}}(\boldsymbol{\Phi}, \boldsymbol{\varphi}, \psi)$ is known for all possible half-angles. Hence, Equation (17) can then be used to reconstruct the integral of the distribution along the line that passes through the first detector element and is perpendicular to the plane that contains both detectors. To avoid a possible misconception, to perform the reconstruction just described, note that the photons interacting with the first detector do not have to emanate from the direction perpendicular to the plane that contains both detectors; rather, the photons can emanate from any direction. From these photons, the integral of the distribution along the line that is perpendicular to the plane that contains both detectors can be reconstructed. Once the integral along this line has been produced, a three-dimensional reconstruction of the distribution can be performed by using conventional tomographic techniques.

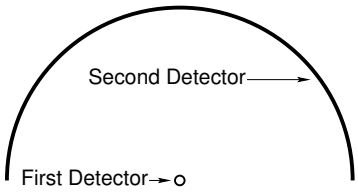

Figure 2. The single first semicircle second (SFSS) camera design consists of a first detector element and a second detector shaped as a semicircle. This figure illustrates that the integral of the integral of cone-beam line-integrals (IILI) model can be implemented. The distribution of radioactivity would lie in front of the plane that contains the detectors.

4.2. Single First Detector Ring Second Detector Design

Sensitivity is defined to be the fraction of the photons that emanate from a radioactive source that are actually detected and used in the image formation process. To produce quality images, it is desirable to develop imaging systems with high sensitivity. The sensitivity of the SFSS design can be approximately doubled. By noting the symmetry involved, Equation (16) can be rewritten as:

$$\mathrm{S}_{\mathrm{IILI}}(\boldsymbol{\Phi}, \boldsymbol{\varphi}, \psi) = \frac{1}{2} \int_{0}^{2\pi} \mathrm{S}_{\mathrm{ILI}}(\boldsymbol{\Phi}, \boldsymbol{\beta}(\theta, \varphi), \psi)\, d\theta \tag{18}$$

This equation allows the second detector of the SFSS design to be extended from a semicircle to a full circle, as illustrated in Figure 3; thus approximately doubling the sensitivity of the design. It could be said that the first detector is "seen" from the second detector in a "circle of directions". This design is referred to as the single first ring second (SFRS) design.

The SFRS camera design can be extended to facilitate the reconstruction of parallel projections. Forming a single larger camera by arranging multiple SFRS cameras in a two-dimensional array would allow a parallel projection of the distribution to be made with just one positioning of the camera. This design, which is illustrated in Figure 4, is referred to here as the multiple single first ring second (MSFRS) design.

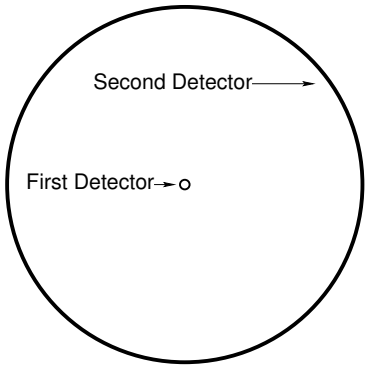

Figure 3. This figure illustrates the single first ring second (SFRS) camera design. The first detector consists of a single first detector element, and the second detector is a coplanar ring centered on the first detector.

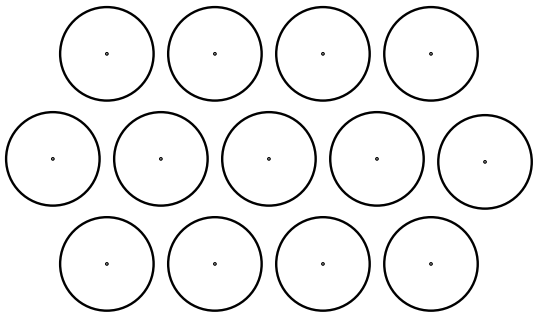

Figure 4. Illustration of the multiple single first ring second (MSFRS) camera design. Multiple SRFS cameras are in a two-dimensional array allowing a parallel projection of the distribution of radioactivity.

To reduce false coincidences, the second detectors could be shielded from the photons emanating from the patient. As is well understood, producing parallel projections as the camera is rotated about the distribution would allow a three-dimensional reconstruction to be made.

4.3. Beach Ball Design: A Camera for Fan-Beam Reconstruction

A fan-beam projection of the distribution of radioactivity can be produced by arranging multiple semicircle-shaped second detectors so they lie on a hemisphere and are centered on a single first detector element. Three such second detectors are illustrated in Figure 5. Using Equation (17) on the data obtained from each second detector allows the integral of the distribution along the line that is perpendicular to the detector and intersects the first detector element to be reconstructed. As seen in Figure 5, the arrangement of the second detector elements results in a set of line-integrals being

reconstructed that are all perpendicular to the line that contains the end points of the second detector elements and intersects the first detector element. This set of line-integrals is a fan-beam projection of the distribution. Since the resulting camera resembles half of a beach ball, this camera design is referred to as the beach ball design.

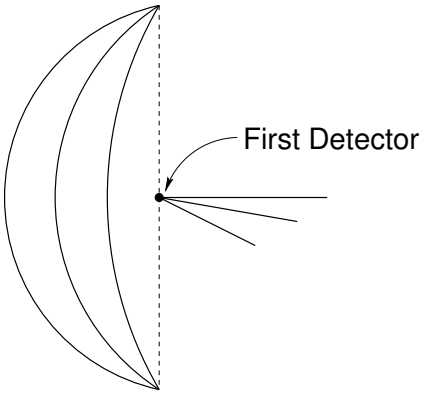

Figure 5. Illustration of the beach ball camera design. In this figure, three multiple semicircle-shaped second detectors are arranged so that they lie on a hemisphere that is centered on a single first detector element. Using Equation (17) on the data obtained from each second detector allows the integral of the distribution along the line that intersects the first detector element and is perpendicular to the plane that contains the second detector to be reconstructed. Three such lines are illustrated in the figure.

The beach ball design can be extended to facilitate a three-dimensional reconstruction of a distribution of radioactivity. If multiple beach balls are arranged as shown in Figure 6 and are rotated about the distribution of radioactivity, then a fan-beam reconstruction can be performed on multiple planes that are perpendicular to the axis of rotation of the motion. This is called the "multiple beach ball" camera design. This design would result in a data collection geometry that is similar to that of the multi-slice fan-beam collimator used in conventional SPECT [41,42]. This design would allow a three-dimensional reconstruction of the distribution of radioactivity to be made.

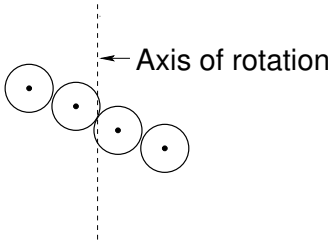

Figure 6. If multiple beach balls are arranged as shown in the figure and rotated about the distribution of radioactivity, then a fan-beam reconstruction can be performed on multiple planes that are perpendicular to the axis of the rotation; thus making a three-dimensional reconstruction possible. In practice, the axis of rotation of the camera would typically be the axis of symmetry of the patient.

5. Methodology of Computer Simulations

Computer simulations were performed to further verify the imaging model and inversion method presented in Section 3. Discrete approximations to the equations presented in Section 3 were made, and computer code was written to implement them. A mathematical phantom, which consists of five constant grayscale ellipsoids, was used in simulating the data. The phantom is similar to a head phantom previously proposed [43]. The ellipsoids are listed in Table 1. For example, the lengths of the semi-principal axes of the ellipsoid that represents the skull's outer boundary are 0.75, 0.75 and 1.00 units. To simulate the reconstruction of line-integrals from Compton camera data, the MSFRS camera design was used. The MSFRS camera consisted of 10^4 coplanar SFSS cameras arranged in a 100×100 rectangular grid and was located 2.2 units from the center of the phantom. For each first and second detector element pair, 46 cone integrals of the distribution, which were equally spaced between 0 and 180 degrees, were calculated. The SFSS cameras were spaced 0.03 units apart. As a consequence, the whole parallel projection of the phantom was reconstructed (e.g., the projection was not truncated). Thus, a total of 10^4 line-integrals was calculated.

Table 1. The five phantoms that comprise the mathematical phantom used in this paper.

Ellipsoid	Origin			Axes			Rotation		Gray Level
	x	y	z	x	y	z	θ_x	θ_z	
Outer skull boundary	0.0	0.0	0.0	0.75	0.75	1.00	0.0	0.0	1.00
Inner skull boundary	0.0	0.0	0.0	0.637	0.637	0.85	0.0	0.0	0.75
Larger ventricle	−0.22	0.0	0.25	0.16	0.30	0.35	0.0	0.0	0.50
Smaller ventricle	0.22	0.0	0.25	0.11	0.17	0.25	0.0	0.0	0.50
Small tumor	0.0	0.0	−0.40	0.1	0.1	0.1	0.0	0.0	0.825

6. Results of Computer Simulations

The results of computer simulations to demonstrate the imaging model and inversion method previously discussed in Section 3 are presented here. A parallel projection of the phantom was reconstructed using the IILI imaging model for the data. To help illustrate the overall accuracy of the projection, the reconstruction is displayed as an image alongside the image of the "true" projection. Furthermore, to illustrate the accuracy of the reconstructed values more quantitatively, the reconstructed line-integral values and the true line-integral values along a one-dimensional slice of the projection through its center are presented in a graph.

The two images in Figure 7 provide a comparison of the "true" parallel projection of the phantom with the reconstructed one. In neither image can all five ellipsoids be seen, because the grayscale values of these images are line-integrals of the phantom, not voxel values. The image on the left is the true parallel projection of the phantom. This projection was obtained by numerically integrating the phantom in the direction collinear to the y-axis. The image on the right is the reconstructed projection. This image is seen to be largely similar to the true image. In particular, no distortion of the boundaries that comprise the image can be seen in the reconstructed projection. In the true image, the ball located at the bottom of the phantom (Ellipsoid 5) is faint, but the lower half is observable. However, this ball cannot be

seen in the reconstructed image. A close inspection of the images reveals some blurring of Ellipsoids 3 and 4. The grayscale windowing values for true image are $[0.85, 1.12]$, and the windowing values for the reconstructed image are $[0.75, 1.07]$.

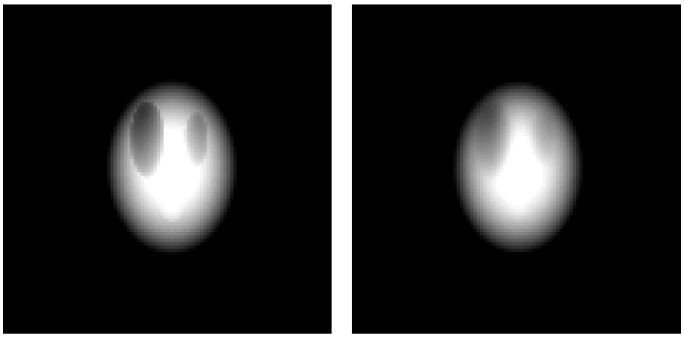

Figure 7. Comparison of the "true" parallel projection (**left**) with the reconstructed projection using the IILI model for the data (**right**). The reconstructed parallel projection is seen to be similar to the true parallel projection. To avoid misinterpreting these images, note that the grayscale values of these images are line-integrals of the phantom not voxel values.

In Figure 8, a graph of the "true" line-integrals values (solid line) of the phantom and a graph of the reconstructed line-integrals values (dashed line) are presented. In particular, the graphs are the values of the line-integrals along the vertical cross-section through the center of the parallel projection. Largely speaking, the two graphs are similar within the support of the phantom, although the graph of the reconstructed values appears to be a smooth version of the graph of the true values. This smoothness is expected given the quadratures used to implement the inversion formulas. Moreover, it can be seen that the reconstructed values are typically lower than the true values with a relative error of about five percent.

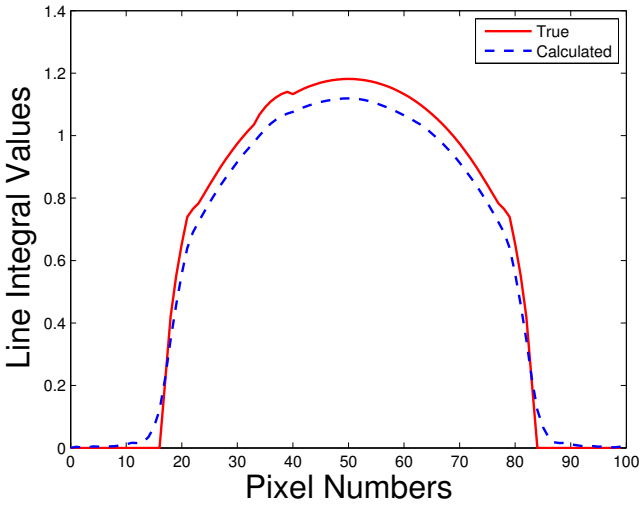

Figure 8. Comparison of the reconstructed line-integrals (dashed line) assuming the IILI model for the data with the "true" line-integrals values (solid line). The reconstructed values are seen to be similar to the true values. The graphs are the values of the line-integrals along the vertical cross-section through the center of the parallel projections shown in Figure 7.

7. Discussion

7.1. Discussion of Camera Designs

7.1.1. MSFRS Camera Design

The MSFRS camera design has advantages and disadvantages. All would agree that the lack of sensitivity would be a major disadvantage of the MSFRS design. Increasing the number of first detectors per area on the face of the camera will improve the sensitivity of the camera. An increase in the density of first detectors on the face of the camera can be achieved in a number of ways. Decreasing the distance between the first and second detectors will make it possible to increase the density of the first detectors on the face of the camera. Stacking and/or overlapping the SFRS cameras that comprise the MSFRS camera can also increase the density. Alternatively, SFSS cameras can be stacked and/or overlapped to form a camera with more sensitivity. However, the amount of stacking that can be achieved in practice is limited by the need to keep the first detectors as close to the distribution of radioactivity as possible to prevent degradation of the camera's accuracy. On the other hand, the MSFRS camera design does have an advantage. A problem with the conventional camera design is the false coincidences caused by gamma rays being scattered from the second detector back into the first detector [44]. An advantage of the MSFRS design is that this source of false coincidences is substantially reduced, in comparison to the conventional camera design, because there are fewer second detector elements for each first detector element in the MSFRS design.

7.1.2. Beach Ball Camera Design

The beach ball design has an advantage and a disadvantage relative to the SFRS design. Since the second detector surrounds the first, the beach ball design has a significant increase in sensitivity relative to the SFRS design. However, this will be at the cost of increased false coincidences caused by gamma rays being scattered from the second detector back into the first detector. Like the MSFRS camera, the sensitivity of the multiple beach ball design can be improved by increasing the number of first detector elements per area on the face of the camera. This can be achieved by reducing the distance between the first detector and the second detector.

A disadvantage that both the beach ball and the MSRFS designs have in common is that the camera has to be moved around the object to perform a three-dimensional reconstruction. Another method for performing a three-dimensional reconstruction from Compton camera data, which does not require the motion of the camera, has been previously proposed [36]. To perform this reconstruction, however, both detectors, which comprise the camera, have to be an "infinitely-extending plane".

7.2. Advantages and Disadvantages of the New Imaging Model and Camera Designs

Initially in this section, the advantages of the new imaging model and camera designs are discussed. Finally, in this section, a major disadvantage of such imaging is discussed.

7.2.1. Mitigating the Effects of the Finite Spatial Resolution of Detectors

It is known that the finite spatial resolution of detectors, the finite energy resolution of detectors and Doppler broadening degrade the performance of Compton cameras. A recent study [33] has found that of these three factors, the finite spatial resolution of the detectors is the dominant degrading factor at a higher medical diagnostic energy level (511 keV). As a consequence, mitigating the effects of the finite spatial resolution of detectors has the potential of significantly improving the performance of Compton cameras. Unfortunately, the camera designs proposed in this paper will not totally eliminate the image degradation due to the finite spatial resolution of the detectors. The finite width of ring detectors and first detector elements will degrade the performance of the cameras. Hence, the imaging model proposed in this paper cannot totally eliminate the degradation due to the finite spatial resolution detectors. Nonetheless, they have the potential to significantly mitigate the degradation.

7.2.2. Reducing the Amount of Data Measured and Improving Its Quality

With the MSFRS camera design, the multiple second detector elements have in effect been combined into one element. This reduction will reduce the amount of data that need to be measured. A number of iterative algorithms have been proposed for reconstruction from Compton camera data [45–49]. The importance of reducing the amount of data that needs to be processed is especially important if an iterative algorithm is used for the reconstruction. Furthermore, the larger measurement bins will result in more photons being counted per bin, thus improving the quality of the measurements.

7.2.3. Increasing the Flexibility of Detector Designs

Using the image model proposed here would provide more flexibility in designing the detectors that comprise a Compton camera. Both microstrip and pixelated detectors could be used to build a Compton camera. A microstrip detector is a detector where a family of narrow parallel strips of electrodes is fabricated on one side of the detector and a second family of strips, which runs orthogonally to the first, is fabricated on the opposite side [50]. The current generated in both families of strips when a photon interacts with the detector is used to determine the point of interaction of the photon. In contrast, when the IILI model is used, a second family of strips along with the associated readout electronics is not needed.

Although reconstructions can be made from beach ball cameras with only one family of strips, there may be an advantage of using beach ball cameras with the conventional two families of strips. Previously-developed completeness conditions imply that a cone-beam projection of the distribution of radioactivity would be obtained from a "double-striped beach ball camera" if the ILI model were assumed for the Compton camera data [38].

A cone-beam projection would provide more information than the fan-beam projection produced from the single-striped beach ball camera. However, it should be noted that the number of counts per measurement bin would be smaller with the double-striped camera than with the single-striped camera.

Alternatively, if pixelated detectors rather than detectors with strips are used to build a Compton camera and if the imaging model proposed here were not used, then to obtain the best possible image quality, the detectors would be fabricated with pixels that are as small as possible. However, if the

imaging model proposed here were used, then the detectors could be fabricated using pixels with the most advantageous size, rather than the smallest size possible. For example, a semicircle detector could be realized by tiling together a number of smaller flat detectors into an approximate semicircle shape. If it is desirable for each flat detector to consist of just one pixel, then the number and the size of the flat detectors could be selected in an advantageous fashion.

7.2.4. An Disadvantage: Loss of Sensitivity

A camera design with relatively poor sensitivity, at best, would result in the need for an increased imaging time and, at worst, would make the design impractical. Although the designs proposed here are intended for imaging photons higher than the 140 keV photons that are presently imaged with collimated Anger cameras, it is informative to compare the sensitivity of the proposed camera to that of the conventional collimated Anger camera. A major loss of sensitivity with the conventional camera equipped with a parallel collimator is that the collimator stops most of the emanating photons that are not approximately perpendicular to the face of the camera. In contrast, the designs proposed here can use any photon that interacts with the first detector no matter from which direction the photon emanated. This is an advantage of the proposed designs over the conventional collimator design. There are at least three aspects of the designs proposed here, however, that limit sensitivity. First, once the photon interacts with the detector, the photon must travel in just the right direction so that it interacts with the second detector. The beach ball design has an advantage over the MSFRS camera in this respect. Secondly, the area of the first detector must be small. The imaging model proposed here assumes its area is infinitesimally small. Thirdly, the number of first detectors per area on the face of the proposed camera limits the sensitivity of the proposed designs. If a photon does not interact with a first detector, the proposed cameras cannot make use of the photon. Unless these aspects are properly addressed, it seems likely that the camera designs proposed here will exhibit inferior sensitivity to that of the conventional collimated Anger camera.

Nonetheless, proposing new Compton camera designs that reduce sensitivity is not without precedent. Equipping Compton cameras with parallel plate collimators [51] and multiple pinhole collimators [52] has been proposed. More recently, equipping Compton cameras with an innovative collimator have been proposed [53]. The collimator has multiple pinholes in its center region and large area slats in its outer region. Unfortunately, the addition of a collimator of any sort will reduce the sensitivity of the camera. The new imaging model proposed here has the potential of mitigating the degradation caused by the finite spatial resolution of detectors, but unfortunately, the camera designs proposed here that can be used to implement the model will significantly reduce the sensitivity of the camera. In the future, more work is needed to determine if the use of the new imaging model will improve the imaging capabilities of Compton cameras despite the loss of sensitivity caused by the use of the new camera designs. Regardless of the outcome of this work, the results presented here illustrate that new models for imaging from Compton scatters are possible and motivates the development of further models that could be more advantageous than the ones already developed.

8. Conclusions

A new imaging model for Compton cameras has been proposed. The model has the potential of mitigating the loss of accuracy due to the finite spatial resolution of detectors, decreasing the amount of data that needs to be processed and simplifying the construction of detectors for Compton cameras. The results of a computer simulation indicate that the new imaging model can produce reasonable images, at least when noiseless simulated data are used. The implementation of the new imaging model, however, requires new camera designs. Unfortunately, the camera designs presented here will result in significant loss in sensitivity in comparison to the conventional parallel planar Compton camera design. In the future, more work is needed to determine if the use of the new imaging model will improve the imaging capabilities of Compton cameras despite the loss of sensitivity caused by the use of the new camera designs. Regardless of the outcome of this work, the results presented here illustrate that new models for imaging from Compton scatters are possible and motivate the development of further models that could be more advantageous than the ones already developed.

Acknowledgments

The author acknowledges the constructive comments made by the anonymous reviewers.

Conflicts of Interest

The author declares no conflict of interest.

References

1. Jurcic, J.G.; Larson, S.M.; Sgouros, G.; McDevitt, M.R.; Finn, R.D.; Divgi, C.R.; Ballangrud, A.M.; Hamacher, K.A.; Ma, D.S.; Humm, J.L.; *et al.* Targeted at particle immunotherapy for myeloid leukemia. *Blood* **2002**, *100*, 1233–1239.
2. Jurcic, J.G.; McDevitt, M.R.; Pandit-Taskar, N.; Divgi, C.R.; Finn, R.D.; Sgouros, G.; Apostalidis, C.; Chanel, S.; Larson, S.M.; Scheinberg, D.A. Alpha-particle immunotherapy for acute myeloid leukemia (AML) with bismuth-213 and actinium-225. *Cancer Biother. Radiopharm.* **2006**, *21*, 40.
3. Rosenblat, T.; McDevitt, M.R.; Mulford, D.A.; Pandit-Taskar, N.; Weiss, M.A.; Heaney, M.L.; Chanel, S.; Morgenstern, A.; Larson, S.M.; Scheinberg, D.A.; *et al.* Sequential Cytarabine and Alpha-Particle Immunotherapy with Bismuth-213 (Bi-213)-Labeled-HuM195 (Lintuzumab) for Acute Myeloid Leukemia (AML). *Blood* **2008**, *112*, 1025–1025.
4. Rosenblat, T.L.; McDevitt, M.R.; Mulford, D.A.; Pandit-Taskar, N.; Divgi, C.R.; Panageas, K.S.; Heaney, M.L.; Chanel, S.; Morgenstern, A.; Sgouros, G.; *et al.* Sequential Cytarabine and alpha-Particle Immunotherapy with Bismuth-213-Lintuzumab (HuM195) for Acute Myeloid Leukemia. *Clin. Cancer Res.* **2010**, *16*, 5303–5311.
5. Pagel, J.M.; Kenoyer, A.L.; Back, T.; Hamlin, D.K.; Wilbur, D.S.; Fisher, D.R.; Park, S.I.; Frayo, S.; Axtman, A.; Orgun, N.; *et al.* Anti-CD45 pretargeted radioimmunotherapy using

bismuth-213: High rates of complete remission and long-term survival in a mouse myeloid leukemia xenograft model. *Blood* **2011**, *118*, 703–711.

6. Ranson, M.; Tian, Z.; Andronicos, N.M.; Rizvi, S.; Allen, B.J. *In vitro* cytotoxicity of bismuth-213 (Bi-213)-labeled-plasminogen activator inhibitor type 2 (alpha-PAI-2) on human breast cancer cells. *Breast Cancer Res. Treat.* **2002**, *71*, 149–159.
7. Allen, B.J.; Tian, Z.; Rizvi, S.M.A.; Li, Y.; Ranson, M. Preclinical studies of targeted alpha therapy for breast cancer using Bi-213-labelled-plasminogen activator inhibitor type 2. *Br. J. Cancer* **2003**, *88*, 944–950.
8. Song, H.; Shahverdi, K.; Huso, D.L.; Esaias, C.; Fox, J.; Liedy, A.; Zhang, Z.; Reilly, R.T.; Apostolidis, C.; Morgenstern, A.; *et al.* Bi-213 (alpha-emitter)-antibody targeting of breast cancer metastases in the neu-N transgenic mouse model. *Cancer Res.* **2008**, *68*, 3873–3880.
9. Lingappa, M.; Song, H.; Thompson, S.; Bruchertseifer, F.; Morgenstern, A.; Sgouros, G. Immunoliposomal Delivery of Bi-213 for alpha-Emitter Targeting of Metastatic Breast Cancer. *Cancer Res.* **2010**, *70*, 6815–6823.
10. Senekowitsch-Schmidtke, R.; Schuhmacher, C.; Becker, K.; Nikula, T.; Seidl, C.; Becker, I.; Miederer, M.; Apostolidis, C.; Adam, C.; Huber, R.; *et al.* Highly specific tumor binding of a Bi-213-labeled monoclonal antibody against mutant E-cadherin suggests its usefulness for locoregional alpha-radioimmunotherapy of diffuse-type gastric cancer. *Cancer Res.* **2001**, *61*, 2804–2808.
11. Bloechl, S.; Beck, R.; Seidl, C.; Morgenstern, A.; Schwaiger, M.; Senekowitsch-Schmidtke, R. Fractionated locoregional low-dose radioimmunotherapy improves survival in a mouse model of diffuse-type gastric cancer using a Bi-213-conjugated monoclonal antibody. *Clin. Cancer Res.* **2005**, *11*, 7070S–7074S.
12. Beck, R.; Seidl, C.; Pfost, B.; Morgenstern, A.; Bruchertseifer, F.; Baum, H.; Schwaiger, M.; Senekowitsch-Schmidtke, R. Bi-213-radioimmunotherapy defeats early-stage disseminated gastric cancer in nude mice. *Cancer Sci.* **2007**, *98*, 1215–1222.
13. Cordier, D.; Forrer, F.; Bruchertseifer, F.; Morgenstern, A.; Apostolidis, C.; Good, S.; Muller-Brand, J.; Macke, H.; Reubi, J.C.; Merlo, A. Targeted alpha-radionuclide therapy of functionally critically located gliomas with Bi-213-DOTA-[Thi(8),Met(O-2)(11)] -substance P: A pilot trial. *Eur. J. Nucl. Med. Mol. Imaging* **2010**, *37*, 1335–1344.
14. Heeger, S.; Moldenhauer, G.; Egerer, G.; Wesch, H.; Martin, S.; Nikula, T.; Apostolidis, C.; Brechbiel, M.W.; Ho, A.D.; Haas, R. Alpha-radioimmunotherapy of B-lineage non-Hodgkin's lymphoma using Bi-213-labelled anti-CD19 and anti-CD20-CHX-A″-DTPA conjugates. *Abstr. Papers Am. Chem. Soc.* **2003**, *225*, U261.
15. Park, S.I.; Shenoi, J.; Pagel, J.M.; Hamlin, D.K.; Wilbur, D.S.; Orgun, N.; Kenoyer, A.L.; Frayo, S.; Axtman, A.; Back, T.; *et al.* Conventional and pretargeted radioimmunotherapy using bismuth-213 to target and treat non-Hodgkin lymphomas expressing CD20: a preclinical model toward optimal consolidation therapy to eradicate minimal residual disease. *Blood* **2010**, *116*, 4231–4239.
16. Knor, S.; Sato, S.; Huber, T.; Morgenstern, A.; Bruchertseifer, F.; Schmitt, M.; Kessler, H.; Senekowitsch-Schmidtke, R.; Magdolen, V.; Seidl, C. Development and evaluation of peptidic ligands targeting tumour-associated urokinase plasminogen activator receptor (uPAR) for use in

alpha-emitter therapy for disseminated ovarian cancer. *Eur. J. Nucl. Med. Mol. Imaging* **2008**, *35*, 53–64.

17. Song, Y.J.; Qu, C.F.; Rizvi, S.M.A.; Li, Y.; Robertson, G.; Raja, C.; Morgenstern, A.; Apostolidis, C.; Perkins, A.C.; Allen, B.J. Cytotoxicity of PAI2, C595 and Herceptin vectors labeled with the alpha-emitting radioisotope Bismuth-213 for ovarian cancer cell monolayers and clusters. *Cancer Lett.* **2006**, *234*, 176–183.
18. Qu, C.F.; Song, E.Y.; Li, Y.; Rizvi, S.M.A.; Raja, C.; Smith, R.; Morgenstern, A.; Apostolidis, C.; Allen, B.J. Pre-clinical study of Bi-213 labeled PAI2 for the control of micrometastatic pancreatic cancer. *Clin. Exp. Metastasis* **2005**, *22*, 575–586.
19. Vervoort, L.; Burvenich, I.; Staelens, S.; Dumolyn, C.; Waegemans, E.; van Steenkiste, M.; Baird, S.K.; Scott, A.M.; de Vos, F. Preclinical Evaluation of Monoclonal Antibody 14C5 for Targeting Pancreatic Cancer. *Cancer Biother. Radiopharm.* **2010**, *25*, 193–205.
20. Drecoll, E.; Gaertner, F.C.; Miederer, M.; Blechert, B.; Vallon, M.; Muller, J.M.; Alke, A.; Seidl, C.; Bruchertseifer, F.; Morgenstern, A.; *et al*. Treatment of Peritoneal Carcinomatosis by Targeted Delivery of the Radio-Labeled Tumor Homing Peptide Bi-213-DTPA-[F3](2) into the Nucleus of Tumor Cells. *PLoS ONE* **2009**, *4*, 1–9.
21. Vallon, M.; Seidl, C.; Blechert, B.; Li, Z.L.; Gilbertz, K.P.; Baumgart, A.; Aichler, M.; Feuchtinger, A.; Gaertner, F.C.; Bruchertseifer, F.; *et al*. Enhanced efficacy of combined Bi-213-DTPA-F3 and paclitaxel therapy of peritoneal carcinomatosis is mediated by enhanced induction of apoptosis and G2/M phase arrest. *Eur. J. Nucl. Med. Mol. Imaging* **2012**, *39*, 1886–1897.
22. Essler, M.; Gärtner, F.C.; Neff, F.; Blechert, B.; Senekowitsch-Schmidtke, R.; Bruchertseifer, F.; Morgenstern, A.; Seidl, C. Therapeutic efficacy and toxicity of 225Ac-labelled vs. 213Bi-labelled tumour-homing peptides in a preclinical mouse model of peritoneal carcinomatosis. *Eur. J. Nucl. Med. Mol. Imaging* **2012**, *39*, 602–612.
23. Rizvi, S.M.A.; Li, Y.; Song, E.Y.J.; Qu, C.F.; Raja, C.; Morgenstern, A.; Apostollidis, C.; Allen, B.J. Preclinical studies of Bismuth-213 labeled plasminogen activator inhibitor type 2 (PAI2) in a prostate cancer nude mouse xenograft model. *Cancer Biol. Ther.* **2006**, *5*, 386–393.
24. McDevitt, M.R.; Barendswaard, E.; Ma, D.; Lai, L.; Curcio, M.J.; Sgouros, G.; Ballangrud, A.M.; Yang, W.H.; Finn, R.D.; Pellegrini, V.; *et al*. An alpha-particle emitting antibody (Bi-213 J591) for radioimmunotherapy of prostate cancer. *Cancer Res.* **2000**, *60*, 6095–6100.
25. Wild, D.; Frischknecht, M.; Morgenstern, A.; Bruchertseifer, F.; Boisclair, J.; Provencher-Bolliger, A.; Maecke, H. An alpha-Particle Emitting Radiopeptide (213Bi-DOTA-PESIN) for therapy of Prostate Cancer. In Proceedings of the SNM's 56th Annual Meeting, Toronto, ON, Canada, 13–17 June 2009; Society of Nuclear Medicine; number 38; Meeting Abstract.
26. Allen, B.J.; Singla, A.A.; Rizvi, S.M.A.; Graham, P.; Bruchertseifer, F.; Apostolidis, C.; Morgenstern, A. Analysis of patient survival in a Phase I trial of systemic targeted alpha-therapy for metastatic melanoma. *Immunotherapy* **2011**, *3*, 1041–1050.
27. Raja, C.; Graham, P.; Rizvi, S.M.A.; Song, E.; Goldsmith, H.; Thompson, J.; Bosserhoff, A.; Morgenstern, A.; Apostolidis, C.; Kearsley, J.; *et al*. Interim analysis of oxicity and response in

phase 1 trial of systemic targeted alpha therapy for metastatic melanoma. *Cancer Biol. Ther.* **2007**, *6*, 846–852.

28. Allen, B.J.; Raja, C.; Rizvi, S.; Li, Y.; Tsui, W.; Graham, P.; Thompson, J.F.; Reisfeld, R.A.; Kearsley, J.; Morgenstern, A.; *et al*. Intralesional targeted alpha therapy for metastatic melanoma. *Cancer Biol. Ther.* **2005**, *4*, 1318–1324.
29. Rizvi, S.M.A.; Qu, C.F.; Song, Y.J.; Raja, C.; Allen, B.J. *In vivo* studies of pharmacokinetics and efficacy of bismuth-213 labeled antimelanoma monoclonal antibody 9.2.27. *Cancer Biol. Ther.* **2005**, *4*, 763–768.
30. Morgenstern, A.; Bruchertseifer, F.; Apostolidis, C.; Giesel, F.; Mier, W.; Haberkorn, U.; Kratochwil, C. Synthesis of 213Bi-DOTATOC for peptide receptor alpha-therapy of GEP-NET patients refractory to beta therapy. *J. Nucl. Med. Meet. Abstr.* **2012**, *53*, 455.
31. Casadevall, A.; Goldstein, H.; Dadachova, E.A. Targeting host cells harbouring viruses with radiolabeled antibodies. *Expert Opin. Biol. Ther.* **2007**, *7*, 595–597.
32. Dadachova, E.A. Bismuth-213 in Radioimmunotherapy of Infectious Diseases. In Proceedings of the SNM's 56th Annual Meeting. Society of Nuclear Medicine, Toronto, ON, Canada, 13–17 June 2009; Society of Nuclear Medicine; number 130; Meeting Abstract.
33. Uche, C.Z. Optimizing Compton Camera Performance. Ph.D. Thesis, The University of Waikato, Hamilton, New Zealand, 2011.
34. Todd, R.W.; Nightingale, J.M.; Everett, D.B. A proposed Gamma camera. *Nature* **1974**, *251*, 132–134.
35. Compton, A.H. A quantum theory of the scattering of x-rays by light elements. *Phys. Rev.* **1923**, *21*, 483–502.
36. Cree, M.J.; Bones, P.J. Towards direct reconstruction from a gamma camera based on Compton scattering. *IEEE Trans. Med. Imaging* **1994**, *13*, 398–407.
37. Parra, L.C. Reconstruction of cone-beam projections from Compton scattered data. *IEEE Trans. Nucl. Sci.* **2000**, *47*, 1543–1550.
38. Smith, B.D. Line-reconstruction from Compton cameras: Data sets and a camera design. *Opt. Eng.* **2011**, *50*, 10.
39. Smith, B.D. Image reconstruction from cone-beam projections: Necessary and sufficient conditions and reconstruction methods. *IEEE Trans. Med. Imaging* **1985**, *4*, 14–28.
40. Smith, B.D. Reconstruction Methods and Completeness Conditions for Two Compton Data Models. *J. Opt. Soc. Am. A* **2005**, *22*, 445–459.
41. Jaszczak, R.J.; Chang, L.T.; Murphy, P.H. Single photon-emission computed-tomography using multi-slice fan beam collimators. *IEEE Trans. Nucl. Sci.* **1979**, *26*, 610–618.
42. Tsui, B.M.W.; Gullberg, G.T.; Edgerton, E.R.; Gilland, D.R.; Perry, J.R.; McCartney, W.H. Design and clinical utility of a fan beam collimator for SPECT imaging of the head. *J. Nucl. Med.* **1986**, *27*, 810–819.
43. Shepp, L.A. Computerized tomography and nuclear magnetic resonance. *J. Comput. Assist. Tomogr.* **1980**, *4*, 94–107.
44. Earnhart, J.R.D. A Compton Camera for Spectroscopic Imaging from 100 keV to 1 MeV. Ph.D. Thesis, North Carolina State University, Raleigh, NC, USA, 1999.

45. Kim, S.M.; Lee, J.S.; Lee, M.N.; Lee, J.H.; Lee, C.S.; Kim, C.H.; Lee, D.S.; Lee, S.J. Two approaches to implementing projector-backprojector pairs for 3D reconstruction from Compton scattered data. *Nucl. Instrum. Methods Phys. Res. Sect. A: Accel. Spectrom. Detect. Assoc. Equip.* **2007**, *571*, 255–258.
46. Kim, S.M.; Lee, J.S.; Lee, C.S.; Kim, C.H.; Lee, M.C.; Lee, D.S.; Lee, S.J. Fully three-dimensional OSEM-based image reconstruction for Compton imaging using optimized ordering schemes. *Phys. Med. Biol.* **2010**, *55*, 5007–5027.
47. Kim, S.M.; Lee, J.S.; Kim, J.H.; Seo, H.; Kim, C.H.; Lee, C.S.; Lee, S.J.; Lee, M.C.; Lee, D.S. Variance-reduction normalization technique for a Compton camera system. *J. Instrum.* **2011**, *6*, doi:10.1088/1748-0221/6/01/C01040.
48. Andreyev, A.; Sitek, A.; Celler, A. Fast image reconstruction for Compton camera using stochastic origin ensemble approach. *Med. Phys.* **2011**, *38*, 429–438.
49. Nguyen, V.G.; Lee, S.J.; Lee, M.N. GPU-accelerated 3D Bayesian image reconstruction from Compton scattered data. *Phys. Med. Biol.* **2011**, *56*, 2817–2836.
50. Knoll, G.F. *Radiation Detection and Measurement*, 2nd ed.; Wiley: New York, NY, USA, 1989.
51. Uritani, A.; Clinthorne, N.; Gormley, J.; LeBlanc, J.; Rogers, W.; Wehe, D.; Wilderman, S. An electronically collimated gamma camera with a parallel plate collimator for Tc-99m imaging. *IEEE Trans. Nucl. Sci.* **1997**, *44*, 894–898.
52. Meng, L.J.; Rogers, W.L.; Clinthorne, N.H.; Fessler, J.A. Feasibility study of Compton scattering enchanced multiple pinhole imager for nuclear medicine. *IEEE Trans. Nucl. Sci.* **2003**, *50*, 1609–1617.
53. Nguyen, C.; Gillam, J.; Brown, J.; Martin, D.; Nikulin, D.; Dimmock, M. Towards Optimal Collimator Design for the PEDRO Hybrid Imaging System. *IEEE Trans. Nucl. Sci.* **2011**, *58*, 639–650.